

Hydrogen oxidation at the Pt–BaZr_{0.1}Ce_{0.7}Y_{0.1}Yb_{0.1}O_{3–δ} (BZCYYb) interface

Cite this: *Phys. Chem. Chem. Phys.*, 2013, **15**, 3820

Wenping Sun,^{ab} Mingfei Liu,^a Shi Feng,^a Wei Liu,^b Hyeon Cheol Park^c and Meilin Liu^{*a}

An asymmetric cell based on a proton conductor, BaZr_{0.1}Ce_{0.7}Y_{0.1}Yb_{0.1}O_{3–δ} (BZCYYb), with a well-defined patterned Pt electrode was prepared to study the kinetics and mechanism of the hydrogen oxidation reaction under typical conditions for fuel cell operation and hydrogen separation, including operating temperature and hydrogen partial pressure. Steady-state polarization curves were carefully analyzed to determine the apparent exchange current density, limiting current density, and charge transfer coefficients. The empirical reaction order, as estimated from the dependence of electrode polarization (R_p) and exchange current density on the partial pressure of hydrogen (P_{H_2}), varied from 0.55 to 0.71. The results indicate that hydrogen dissociation contributes the most to the rate-limiting step of the hydrogen oxidation reaction taking place at the Pt–BZCYYb interface. At high current densities, surface diffusion of electroactive species appears to contribute to the rate-limiting step as well.

Received 27th November 2012,
Accepted 21st January 2013

DOI: 10.1039/c3cp44225j

www.rsc.org/pccp

1. Introduction

Hydrogen is the cleanest fuel that has great potential to replace fossil-based fuels; however, the high cost of hydrogen production hinders its broad commercialization. As a low energy cost process, membrane technology is very promising for separating hydrogen from product gases, which are generated by reforming or gasification of coal, fossil fuels and biomass. In particular, cermet membranes composed of a ceramic proton conductor and a metallic electronic conductor (*e.g.*, nickel) can be used to extract pure hydrogen from gas mixtures without the need for electrodes or external circuits.^{1–4} Moreover, compared to the most investigated palladium-based membranes, the cermet membranes are more cost-effective and durable. Thus, the cermet membranes have attracted more and more attention. The widely accepted mechanism for hydrogen permeation through the cermet membranes is described as below.⁵ First, hydrogen gas molecules are adsorbed, dissociated, and ionized on a membrane surface, producing protons and electrons at the

metal–ceramic interface (higher H₂ partial pressure side of the dense cermet membrane). Second, the protons move through the ceramic phase (proton conductor) or the metal–ceramic interface, whereas the electrons move through the metallic phase (porous 3D network) of the cermet membrane to the lower H₂ partial pressure side of the dense cermet membrane, driven by a chemical potential gradient across the membrane. Finally, protons and electrons recombine to form hydrogen gas molecules at the lower H₂ partial pressure side of the membrane.

As a high-efficiency energy conversion electrochemical device, solid oxide fuel cells (SOFCs) can utilize a proton conductor as an electrolyte to directly convert chemical energy into electricity, which have been widely studied in the past decade.^{6,7} In proton-conducting SOFCs fueled with hydrogen, hydrogen molecules dissociate into protons and electrons in the anode zone; then, protons transport through the proton-conducting electrolyte to the cathode zone as electrons travel to the cathode *via* an external circuit. Finally, the protons react with oxygen, generating water in the cathodic compartment of the fuel cell.^{8,9} For both hydrogen separation and SOFC operation, hydrogen oxidation is an important step of the electrochemical processes. The rate of the hydrogen oxidation reaction determines the hydrogen permeation rate of separation membranes and the electrochemical performance of the SOFCs. Therefore, it is vital to gain a fundamental understanding of the mechanism and kinetics of the hydrogen oxidation reaction in order to design high-performance materials/novel architectures for these applications.¹⁰

^a Center for Innovative Fuel Cell and Battery Technologies, School of Materials Science and Engineering, Georgia Institute of Technology, Atlanta, GA 30332, USA. E-mail: meilin.liu@mse.gatech.edu; Fax: +1 404 894 9140; Tel: +1 404 894 6114

^b CAS Key Laboratory of Materials for Energy Conversion, Department of Materials Science and Engineering, University of Science and Technology of China (USTC), Hefei 230026, P. R. China

^c Advanced Materials Research Center, Samsung Advanced Institute of Technology (SAIT), San 14-1, Nongseo-dong, Yongin-si 446-712, Republic of Korea

Acceptor-doped cerate and zirconate perovskite oxides are the state-of-the-art proton conductors.¹¹ Among the perovskite oxides investigated, acceptor-doped cerates show high proton conductivity, but they exhibit poor chemical stability against CO₂ or water vapor. Unlike cerates, zirconates showed high chemical stability, but displayed limited proton conductivity and poor sintering ability to dense samples. Recently, our group has developed an Y and Yb co-doped BaCeO₃–BaZrO₃ proton conductor, BaZr_{0.1}Ce_{0.7}Y_{0.1}Yb_{0.1}O_{3–δ} (BZCYYb), which has relatively high ionic conductivity and reasonable stability under atmospheres containing 50 vol% of CO₂ and water vapor.⁷ Additionally, it has been demonstrated that Ni–BZCYYb anodes exhibit excellent tolerance to sulfur poisoning and coking under fuel cell operating conditions. BZCYYb turns out to be a very promising proton conductor for proton-conducting SOFCs and hydrogen separation membranes. Therefore, we used BZCYYb as a proton-conducting phase in a metal–BZCYYb composite membrane to investigate the hydrogen oxidation reaction in this work.

While the hydrogen oxidation reaction at metal–proton conductor interfaces has been investigated, a clear understanding of the hydrogen oxidation kinetics and mechanism is still lacking, especially at the Pt–BZCYYb interface. In particular, the results reported in the literature are not consistent; there is still a dispute on which elementary step is the rate-limiting step of the hydrogen oxidation reaction. Further, electrochemical results strongly depend on the cell design, electrolyte and electrode materials used, and the measurement conditions. Thus, it is also difficult to compare the data collected under different conditions. In most cases, SrCeO₃-based oxides were used as the proton-conducting phase. Bonanos and Mogensen¹² investigated the anodic polarization behavior at the Ni–Sr_{0.995}Ce_{0.95}Y_{0.05}O_{2.975} interface using a Ni electrode (with a point contact) in a three-electrode cell, and claimed that the rate determining step might be diffusion of a simple species such as dissociated hydrogen. D. Kek *et al.*^{13–15} studied the effect of electrode material and H–D isotope effect on the electrode kinetics of the metal–Sr_{0.995}Ce_{0.95}Y_{0.05}O_{2.97} interface. The electrochemical measurements were also performed with metal electrodes (with a point contact) in three-electrode cells. They found that the hydrogen oxidation reaction mechanism is determined by the nature of the electrode material and hydrogen isotopes, rather than the electrolyte surface. They also proposed that the rate-limiting step is dependent on the electrode material. Zisekas *et al.* investigated the electrode kinetics at the Pd–proton conductor interface, where a porous Pd film was used as an electrode.¹⁶ SrCe_{0.95}Yb_{0.05}O_{3–a} and SrZr_{0.95}Y_{0.05}O_{3–a} were used as proton conductors. They concluded that the electrode kinetics is dependent on the proton-conducting phase and is much faster at the Pt–SrCe_{0.95}Yb_{0.05}O_{3–a} interface. Akoshima *et al.*¹⁷ evaluated the electrode reaction at the porous Pt electrode–BaCe_{0.95}Y_{0.05}O_{3–δ} interface, and the surface diffusion combined with dissociative adsorption of hydrogen species near the triple phase boundary (TPB) was considered to be the rate-limiting step.

In this study, we investigated the hydrogen oxidation reaction at a Pt–BZCYYb interface. An asymmetric cell was designed

to perform the electrochemical measurements. One side of the cell is a porous, highly-active Pt counter electrode (CE); the other side is a well-defined patterned Pt working electrode (WE). Since the TPB length (active sites) of the CE is several orders of magnitude longer than that of the WE, the contribution of the CE to the polarization behavior of the cell is insignificant and hence can be ignored. Thus, the porous Pt electrode was used as both the CE and the reference electrode (RE). By applying a positive bias to the patterned Pt electrode with respect to the CE, hydrogen oxidation would be the predominant electrochemical reaction on the patterned Pt electrode (WE). The aim of the present work is to investigate the hydrogen oxidation reaction at the Pt–BZCYYb interface experimentally to gain some further insight into the related reaction behavior in hydrogen separation membranes and proton-conducting SOFCs.

2. Experimental

2.1. Sample preparation and characterization

BaZr_{0.1}Ce_{0.7}Y_{0.1}Yb_{0.1}O_{3–δ} (BZCYYb) powders were synthesized by a typical solid-state reaction method.⁷ The Pt patterned electrode was prepared by first pressing a Pt mesh into the middle of a BZCYYb green pellet,¹⁸ and then sintering at 1500 °C for 10 h in a 5% H₂–Ar atmosphere. The sintered dense pellet was subsequently ground until the Pt mesh was partially exposed, followed by polishing and cleaning. The diameter and thickness of the final sample was about 11.5 and 0.60 mm, respectively. The dimension of the Pt mesh was about 5 mm × 5 mm. Pt paste was brush-painted onto the other side of the BZCYYb pellet followed by firing at 900 °C for 2 h. Subsequently, 0.05 mol L^{–1} Pt(NH₃)₄(NO₃)₂ solution was infiltrated into the porous Pt electrode and fired at 750 °C for 1 h, resulting in an asymmetric cell based on a BZCYYb electrolyte with a Pt patterned electrode. The morphology of the Pt patterned electrode was examined using a thermally assisted field emission scanning electron microscope (SEM, LEO 1530).

2.2. Electrochemical measurements

The electrochemical properties of the sample with a Pt patterned electrode were measured in a testing apparatus schematically shown in Fig. 1. An EG&G PAR potentiostat (model 273A) coupled with a Solartron 1255 HF frequency response analyzer was used to acquire the electrochemical impedance spectra (EIS) of the cells in a frequency range from 100 kHz to 0.01 Hz with an AC amplitude of 10 mV. The hydrogen partial pressure was controlled between 0.03 and 1 atm by using N₂ as the diluent. The patterned Pt working electrode (WE) was polarized with respect to the porous Pt counter electrode by applying a potential in the range from 0 to 1 V. The steady-state polarization current was constructed by the cell current at each applied cell voltage. The electrode overpotential was calculated by subtracting the ohmic drop due to the BZCYYb electrolyte resistance from the applied potential between WE and CE.

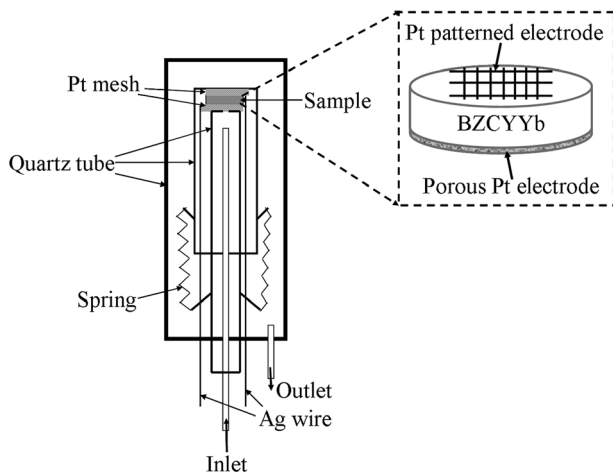


Fig. 1 Schematic of the electrochemical testing apparatus.

3. Results and discussion

3.1. Morphology of Pt patterned electrode

Fig. 2 shows the SEM images of a Pt-patterned electrode embedded in a BZCYYb electrolyte. The dark grey area is the BZCYYb electrolyte, while the light grey area is the Pt patterned electrode. The Pt–BZCYYb interfaces can be readily observed. The contact between Pt and BZCYYb is very good, forming a well-defined triple phase boundary (TPB).

3.2. Electrochemical impedance spectra under open circuit voltage (OCV)

Fig. 3 shows the typical electrochemical impedance spectra (EIS) of the cells measured at different partial pressures of hydrogen at 600 °C under OCV conditions. The ohmic resistance of the cell, which is mainly associated with the electrolyte resistance, is determined from the intercept of the impedance curve with the real axis at high frequencies. The polarization resistance (R_p) of the cell is estimated from the difference between the two intercepts of the impedance curve with the real axis at high and low frequencies. As can be seen, the ohmic resistance of the cell increased gradually as the partial pressure of hydrogen (P_{H_2}) was reduced, suggesting that the proton conductivity of the BZCYYb electrolyte decreased with decreasing partial pressure of hydrogen. Further, the electrode polarization of

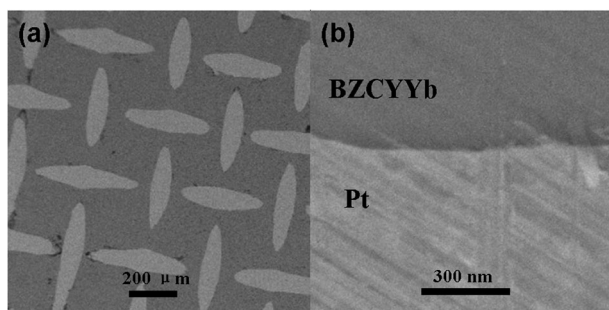
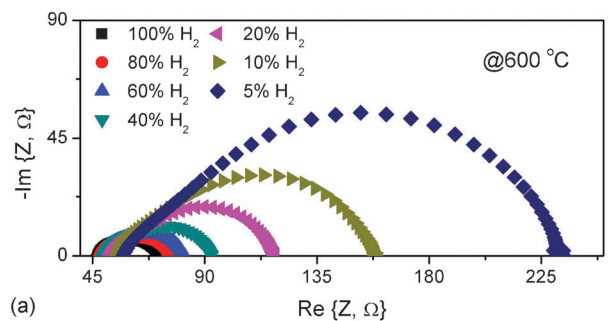
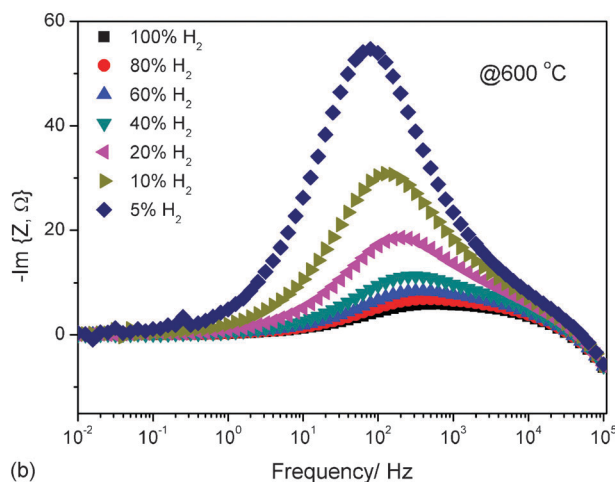


Fig. 2 SEM images of the Pt-patterned electrode embedded in a BZCYYb electrolyte (a) and the interface between Pt and BZCYYb (b).



(a)



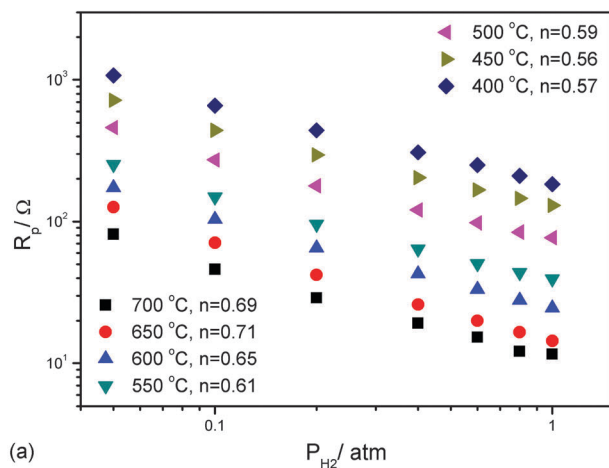
(b)

Fig. 3 Electrochemical impedance spectra (EIS) of the cell measured at different hydrogen partial pressures at 600 °C under OCV conditions. (a) Nyquist plot, (b) variation in imaginary part of impedance.

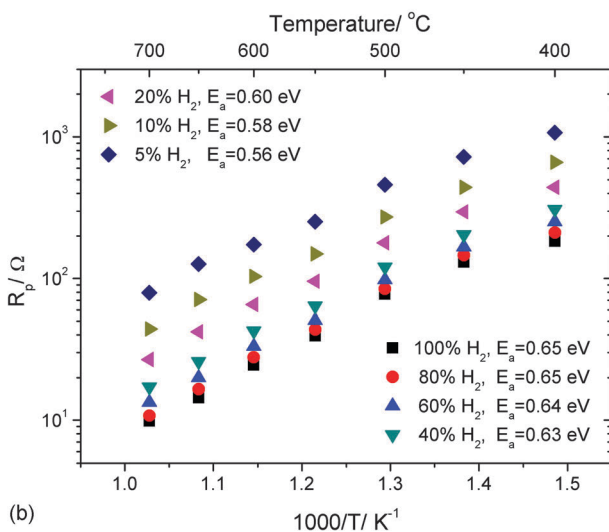
the cell, R_p value, increased significantly with decreasing P_{H_2} . As expected, the frequencies at which the imaginary parts of the impedances reached maximum up-shifted with hydrogen partial pressure (Fig. 3b), indicating that the characteristic relaxation time for the electrode processes decreased with increasing P_{H_2} , or electrode reactions became faster at higher partial pressure of hydrogen.

When the R_p values are plotted logarithmically against P_{H_2} , as shown in Fig. 4(a), the empirical reaction order for the hydrogen oxidation reaction, n , can be estimated from the slope of the linear plots.^{13,14} Ideally, n should be 0.5 if hydrogen dissociation is the rate-limiting step, and 1 if surface diffusion is the rate-limiting step. In the present case, the reaction order with respect to P_{H_2} varies between 0.56 and 0.71, indicating that hydrogen dissociation contributes the most to the rate-limiting step of the hydrogen oxidation reaction. Besides, surface diffusion of hydrogen species may also contribute to the rate-limiting step. The dependence of R_p on temperature at different partial pressures of hydrogen was also plotted, as shown in Fig. 4(b). The apparent activation energy E_a values, calculated from the slopes of the plots, vary from 0.56 to 0.65 eV under atmospheres with different P_{H_2} . The similar E_a values imply that the mechanism of the hydrogen oxidation reaction remained unchanged at different hydrogen partial pressures.

We have also studied the effect of water vapor on the polarization behavior of the cells. The R_p values of a cell as a



(a)



(b)

Fig. 4 (a) Dependence of R_p on P_{H_2} at various operating temperatures. (b) Temperature dependence of R_p at different hydrogen partial pressures.

function of water vapor partial pressure (P_{H_2O}) at 700, 600, and 500 °C are shown in Fig. 5. It can be seen that R_p is independent of P_{H_2O} in the P_{H_2O} range studied; this is consistent with a previous study of a porous Pt electrode– $BaCe_{0.95}Y_{0.05}O_{3-\delta}$ system by Akoshima *et al.*¹⁷ Additionally, they also found that R_p was independent of P_{H_2O} in a wider range at other lower hydrogen partial pressures. This behavior suggests that the hydrogen oxidation reaction is insensitive to water vapor at low partial pressures of water vapor. It was reported that the hydrogen permeation flux through a Ni– $BaZr_{0.1}Ce_{0.7}Y_{0.2}O_{3-\delta}$ (BZCY) membrane became larger when the fed gas was switched from dry to wet H_2 ^{1,19} because the presence of water vapor enhanced the proton conductivity of the BZCY phase, without altering the catalytic activity of the surface.

3.3. Electrochemical impedance spectra under steady-state polarization

Fig. 6 shows some typical impedance spectra of the cell acquired under a DC anodic polarization at 600 °C in 100% H_2 ; the voltage represents a positive bias applied to the Pt

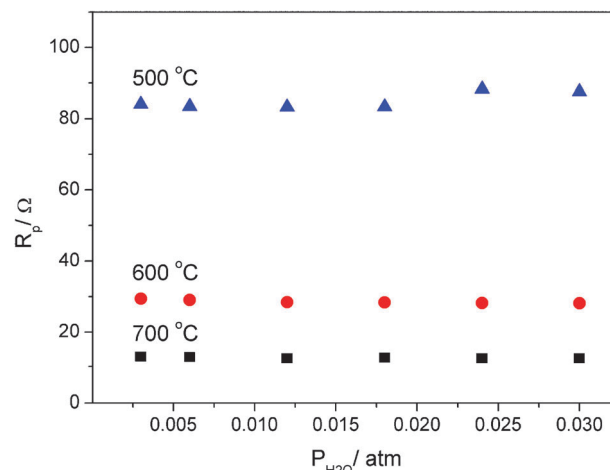
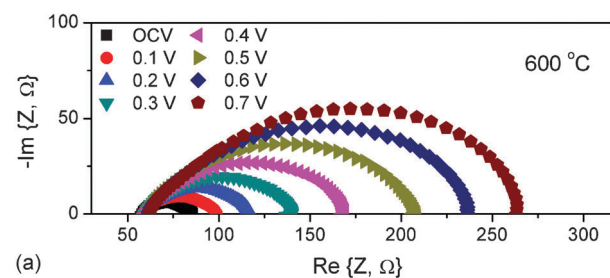
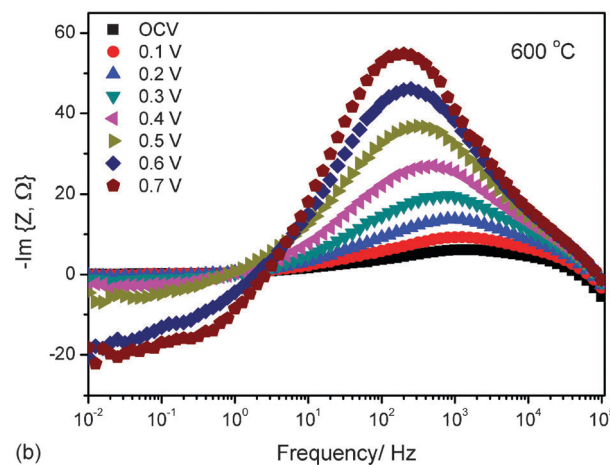


Fig. 5 R_p value of the cell as a function of water vapor partial pressure at 700, 600, and 500 °C.



(a)



(b)

Fig. 6 Typical impedance spectra of a cell acquired when a different positive bias is applied to the Pt electrode at 600 °C in 100% H_2 . (a) Nyquist plot, (b) variation in imaginary part of impedance.

patterned electrode with respect to the CE/RE. When a positive bias is applied, the polarization resistance increased with the amplitude of the positive bias, suggesting that the rate-limiting step of the hydrogen oxidation reaction is not a charge transfer process. This is in good agreement with what was observed for a porous Pt electrode– $BaCe_{0.95}Y_{0.05}O_{3-\delta}$ interface.¹⁷ Besides, the frequencies at which the imaginary parts of the impedances reached maximum down-shifted with increasing positive bias

(Fig. 6b), indicating that the characteristic relaxation time for the electrode processes increased with the positive bias, or electrode reactions were slowed down at higher DC anodic polarization.

The electrode overpotential was estimated by subtracting the ohmic drop of the BZCYYb electrolyte from the applied voltage between the WE and the CE/RE.

When the overall reaction rate is controlled by a charge transfer step, the relationship between the current density passing through the electrode–electrolyte interface, I , and the overpotential across the interface, η , can be approximated by the Butler–Volmer equation:²⁰

$$I = I_0 \left[\exp\left(\frac{\alpha_a F \eta}{RT}\right) - \exp\left(-\frac{\alpha_c F \eta}{RT}\right) \right] \quad (1)$$

where I_0 is the exchange current density, α_a and α_c are the anodic and cathodic transfer coefficients, respectively, F is Faraday's constant, and R is the universal gas constant. When the anodic η values are sufficiently small, the Butler–Volmer equation can be approximated as:

$$I = I_0 \frac{(\alpha_a + \alpha_c) F \eta}{RT} \quad (2)$$

When the anodic η values are sufficiently large, on the other hand, the Butler–Volmer equation can be approximated by the Tafel equation:

$$\ln I = \ln I_0 + \alpha_a \frac{F}{RT} \eta \quad (3)$$

When the rate of mass transport cannot keep up with the rate of the charge-transfer step, the η – I relationship can be described by a modified Butler–Volmer equation:

$$I = I_0 \left[\left(1 - \frac{I}{I_{l,a}}\right) \exp\left(\frac{\alpha_a F \eta}{RT}\right) - \left(1 - \frac{I}{I_{l,c}}\right) \exp\left(-\frac{\alpha_c F \eta}{RT}\right) \right] \quad (4)$$

where $I_{l,a}$ and $I_{l,c}$ are the anodic and cathodic limiting current density, respectively. For high anodic overpotentials, the equation can be approximated by the Tafel equation:

$$\eta = \left(-\frac{RT}{\alpha_a F}\right) \left[\ln\left(\frac{I_{l,a} - I}{I}\right) + \ln\left(\frac{I_{0,a}}{I_{l,a}}\right) \right] \quad (5)$$

Fig. 7 shows the dependence of the current density on the overpotential (Tafel plots) at different temperatures in 100% H₂. It can be seen that these plots are not linear in a wide temperature range (400 to 750 °C), suggesting that mass transport effect cannot be neglected in the hydrogen oxidation reaction. It should also be noted that the mass transport effect varies with the operating temperature.

As mass transport plays an important role under high anodic overpotential (higher than 150 mV), the relationship between the overpotential and current density was fitted with eqn (5). The values of exchange current density ($I_{0,a}$), anodic limiting current density ($I_{l,a}$), and anodic charge transfer coefficient (α_a), as shown in Table 1, depend on the operating temperature. It appears that they increased with the increase in operating temperature. Actually, the values of these parameters were influenced by temperature, hydrogen partial pressure, the nature

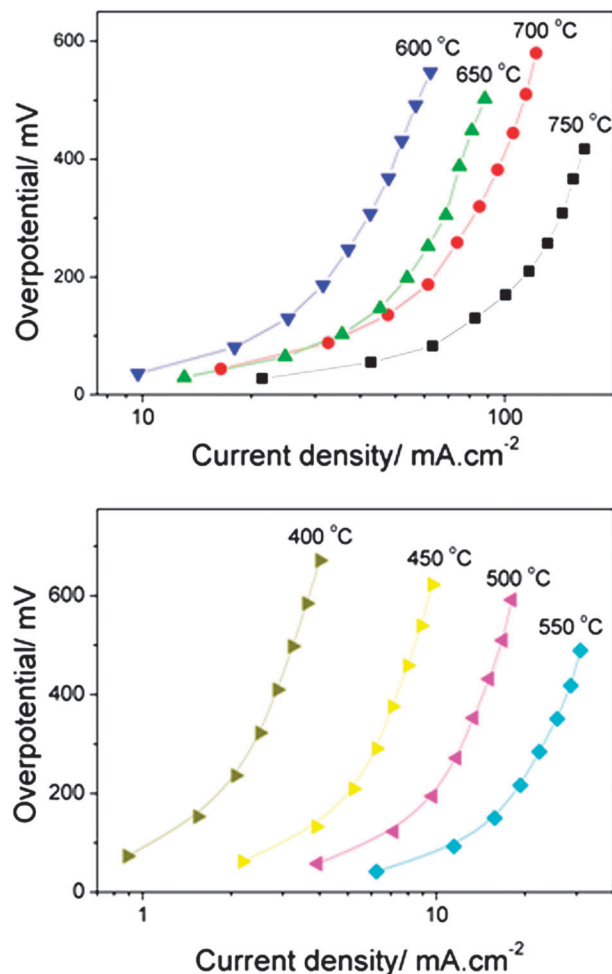


Fig. 7 The dependence of current density on the overpotential of a cell exposed to 100% H₂.

Table 1 The values of exchange current density ($I_{0,a}$), anodic limiting current density ($I_{l,a}$), and anodic charge transfer coefficient (α_a) at different temperatures estimated from fitting the data obtained from high polarization into eqn (5)

Temperature/°C	750	700	650	600	550	500	450	400
$I_{0,a}/\text{mA cm}^{-2}$	66.8	41.8	40.4	24.1	14.9	8.44	4.45	1.64
$I_{l,a}/\text{mA cm}^{-2}$	190.8	146.8	108.7	90.8	69.2	30.6	19.2	8.59
α_a	0.62	0.41	0.38	0.29	0.20	0.19	0.15	0.13

of the electrolyte and electrode, and the electrolyte–electrode interface.^{13,21} To further verify the fitting results, the values of the overpotential and current density obtained at low anodic polarization were fitted into eqn (2) to estimate the corresponding $I_{0,a}(\alpha_a + \alpha_c)$ at different temperatures, as shown in Table 2. Ideally, the value of $\alpha_a + \alpha_c$ should be 1. The values of $I_{0,a}$ determined from this fitting are very close to those estimated from eqn (5), suggesting that the fitting results are reasonable.

The dependence of $I_{0,a}$ and $I_{l,a}$ on temperature is shown in Fig. 8. As expected, the apparent activation energy E_a can be calculated from the slopes of the linear plots. The E_a values are 0.68 eV and 0.59 eV for $I_{0,a}$ and $I_{l,a}$, respectively, which are very close to those estimated from the dependence of R_p on

Table 2 The values of $I_{o,a}(\alpha_a + \alpha_c)$ at 750, 700, 650, and 600 °C estimated from fitting the data obtained from low polarization into eqn (2)

Temperature/°C	750	700	650	600
$I_{o,a}(\alpha_a + \alpha_c)/\text{mA cm}^{-2}$	67.5	30.9	30.2	16.6

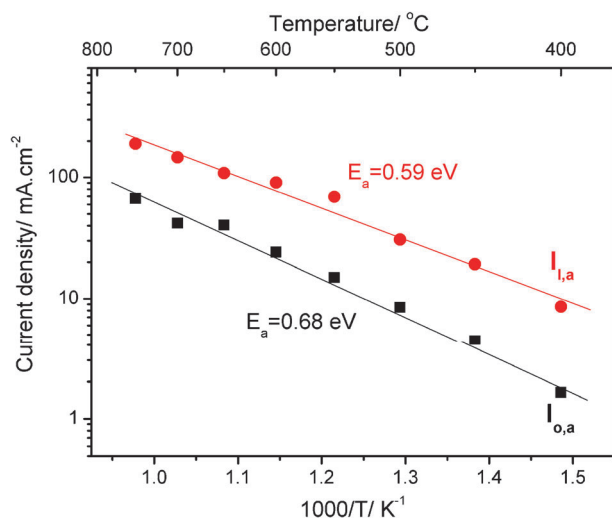


Fig. 8 The dependence of $I_{o,a}$ and $I_{l,a}$ on operating temperature.

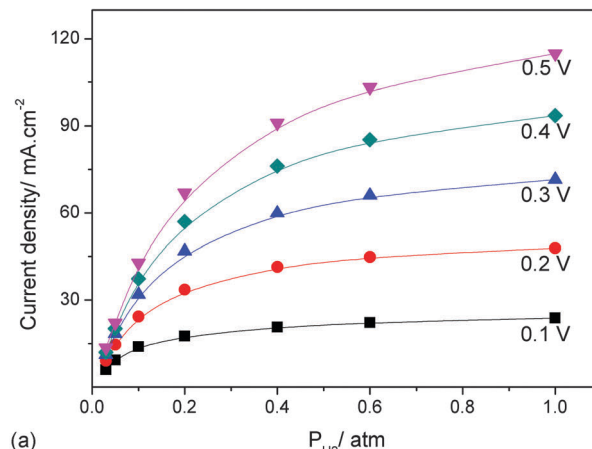
temperature as discussed earlier. It is also noted that similar results were obtained for hydrogen oxidation at other metal–proton conductor interfaces. D. Kek *et al.*¹³ investigated hydrogen oxidation at various metal– $\text{Sr}_{0.995}\text{Ce}_{0.95}\text{Y}_{0.05}\text{O}_{2.97}$ interfaces, the E_a values for $I_{l,a}$ were about 0.70, 1.0, 0.60, and 0.74 eV for Ni, Ag, Cu, and Pt electrode, respectively. S. Zisekas *et al.* reported that the E_a value for $I_{o,a}$ was about 0.65 eV at a Pd– $\text{SrCe}_{0.95}\text{Y}_{0.05}\text{O}_{3-\delta}$ interface, where a porous Pd film was used as an electrode.²² In fact, the activation energy strongly depends on the type and morphology of electrodes.

3.4. Dependence of steady-state polarization on hydrogen partial pressure

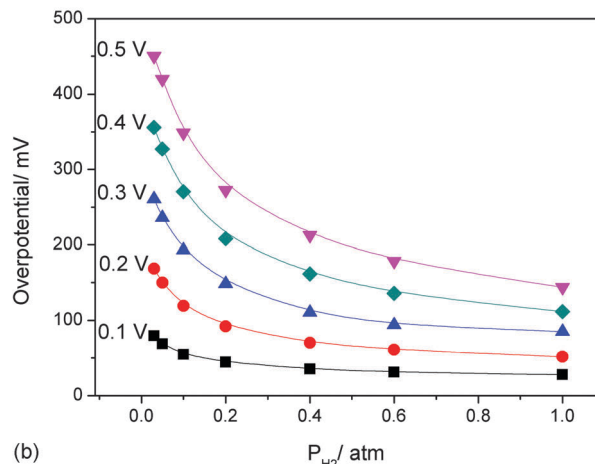
The anodic current densities and overpotentials of the cells measured at different anodic polarizations applied to the Pt patterned electrode exposed to different hydrogen partial pressures at 750 °C are shown in Fig. 9(a) and (b), respectively. The anodic current density increased with the positive bias and hydrogen partial pressure. The overpotential increased with the positive bias but decreased with increasing hydrogen partial pressure. On the other hand, the overpotential at a given current density was increased as the hydrogen partial pressure was reduced, as shown in Fig. 9(c).

The measured overpotentials (higher than 150 mV) and the current densities under different hydrogen partial pressures were fitted into eqn (5) to determine the values of $I_{o,a}$, $I_{l,a}$, and α_a . As expected, both $I_{o,a}$ and $I_{l,a}$ increased with the partial pressure of hydrogen (see Table 3), whereas the anodic charge transfer coefficient α_a remained relatively constant.

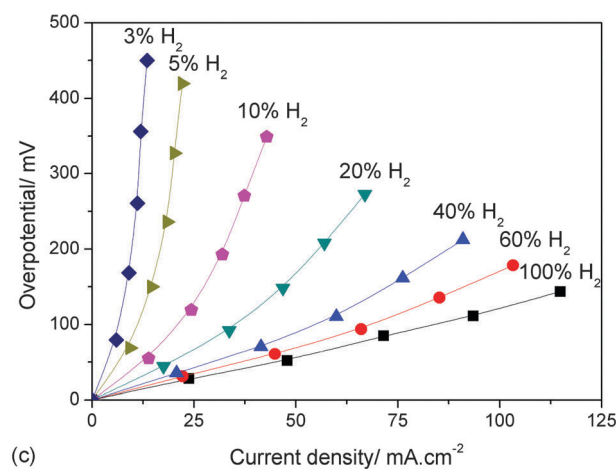
To gain more insights into the kinetics of the hydrogen oxidation reaction, the current densities were plotted as a



(a)



(b)



(c)

Fig. 9 The anodic current density and overpotential of the Pt electrode at different hydrogen partial pressures and positive potential (a and b), and the dependence of overpotential on the anodic current density (c) at 750 °C.

function of P_{H_2} , as shown in Fig. 10. The empirical reaction order, n , can be calculated from the slopes of the straight lines, similar to that calculated from the dependence of R_p on P_{H_2} . The reaction order is about 0.55 and 0.69 for exchange and limiting currents, respectively, which is in good agreement with the values estimated from the dependence of R_p on P_{H_2} , further

Table 3 The values of exchange current density ($i_{o,a}$), anodic limiting current density ($i_{l,a}$), and anodic charge transfer coefficient (α_a) at different hydrogen partial pressures (P_{H_2})

P_{H_2}	100% H_2	10% H_2	5% H_2	3% H_2
$i_{o,a}/\text{mA cm}^{-2}$	66.8	19.6	13.2	9.49
$i_{l,a}/\text{mA cm}^{-2}$	190.8	51.7	24.2	16.7
α_a	0.62	0.64	0.62	0.39

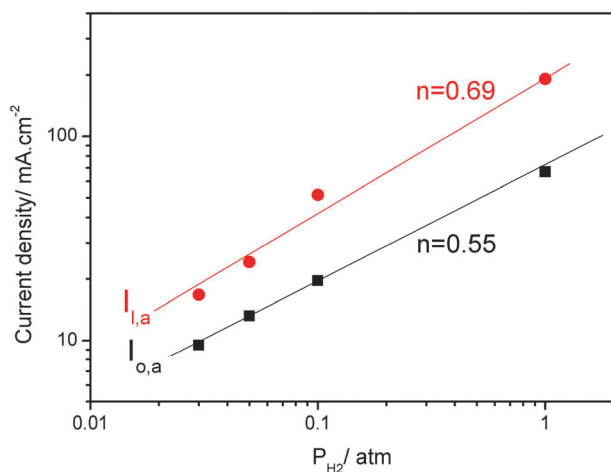


Fig. 10 The dependence of $i_{o,a}$ and $i_{l,a}$ on hydrogen partial pressure.

confirming that hydrogen dissociation contributes more to the rate-limiting step of the reaction.

4. Conclusion

The hydrogen oxidation reaction taking place at a Pt-BZCYYb interface was carefully studied using steady-state polarization measurements. The apparent exchange current density, limiting current density, and charge transfer coefficients of the reaction were calculated from the dependence of the steady-state current-overpotential polarization curves. Further, the apparent reaction order was also estimated from the dependence of R_p on P_{H_2} and exchange/limiting current density on P_{H_2} . The results suggest that the hydrogen dissociation step is the rate-limiting step of the hydrogen oxidation reaction at the Pt-BZCYYb interface at low polarization, but mass transfer starts to contribute to limiting the overall reaction rate at moderate polarization. The effect of mass transfer becomes more pronounced at higher polarization (or current densities).

Acknowledgements

This material is based on work supported by the Samsung Advanced Institute of Technology and as part of the

Heterogeneous Functional Materials (HetroFoam) Center, an Energy Frontier Research Center funded by the U.S. Department of Energy, Office of Science, Office of Basic Energy Sciences, under Award Number DE-SC0001061. W.P. Sun would like to acknowledge a fellowship from the China Scholarship Council.

References

- 1 C. D. Zuo, S. E. Dorris, U. Balachandran and M. L. Liu, *Chem. Mater.*, 2006, **18**, 4647–4650.
- 2 C. D. Zuo, T. H. Lee, S. E. Dorris, U. Balachandran and M. L. Liu, *J. Power Sources*, 2006, **159**, 1291–1295.
- 3 S. M. Fang, L. Bi, X. S. Wu, H. Y. Gao, C. S. Chen and W. Liu, *J. Power Sources*, 2008, **183**, 126–132.
- 4 Z. W. Zhu, W. P. Sun, L. T. Yan, W. F. Liu and W. Liu, *Int. J. Hydrogen Energy*, 2011, **36**, 6337–6342.
- 5 J. W. Phair and S. P. S. Badwal, *Ionics*, 2006, **12**, 103–115.
- 6 C. D. Zuo, S. W. Zha, M. L. Liu, M. Hatano and M. Uchiyama, *Adv. Mater.*, 2006, **18**, 3318–3320.
- 7 L. Yang, S. Z. Wang, K. Blinn, M. F. Liu, Z. Liu, Z. Cheng and M. L. Liu, *Science*, 2009, **326**, 126–129.
- 8 F. Lefebvre-Joud, G. Gauthier and J. Mougins, *J. Appl. Electrochem.*, 2009, **39**, 535–543.
- 9 B. H. Rainwater, M. F. Liu and M. L. Liu, *Int. J. Hydrogen Energy*, 2012, **37**, 18342–18348.
- 10 M. L. Liu, M. E. Lynch, K. Blinn, F. M. Alamgir and Y. Choi, *Mater. Today*, 2011, **14**, 534–546.
- 11 K. D. Kreuer, *Annu. Rev. Mater. Res.*, 2003, **33**, 333–359.
- 12 N. Bonanos and M. Mogensen, *Solid State Ionics*, 1997, **97**, 483–488.
- 13 D. Kek, N. Bonanos, M. Mogensen and S. Pejovnik, *Solid State Ionics*, 2000, **131**, 249–259.
- 14 D. Kek and N. Bonanos, *Solid State Ionics*, 1999, **125**, 345–353.
- 15 D. Kek and N. Bonanos, *Vacuum*, 2001, **61**, 453–457.
- 16 S. Zisekas, G. Karagiannakis and M. Stoukides, *Solid State Ionics*, 2005, **176**, 2929–2934.
- 17 S. Akoshima, M. Oishi, K. Yashiro, K. Sato and J. Mizusaki, *Solid State Ionics*, 2010, **181**, 240–248.
- 18 K. S. Blinn, X. X. Li, M. F. Liu, L. A. Bottomley and M. L. Liu, *J. Visualized Exp.*, 2012, **67**, e50161.
- 19 S. M. Fang, J. Yang, C. S. Chen and W. Liu, *Key Eng. Mater.*, 2008, **368–372**, 256–258.
- 20 G. Pekridis, K. Kalimeri, N. Kaklidis, C. Athanasiou and G. Marnellos, *Solid State Ionics*, 2007, **178**, 649–656.
- 21 G. Pekridis, K. Kalimeri, N. Kaklidis, C. Athanasiou and G. Marnellos, *Solid State Ionics*, 2007, **178**, 649–656.
- 22 S. Zisekas, G. Karagiannakis, M. Ouzounidou, A. Skodra and M. Stoukides, *Ionics*, 2003, **9**, 115–121.